AGU ADVANCING EARTH AND SPACE SCIENCES

Geophysical Research Letters®

RESEARCH LETTER
10.1029/2023GL103429

Special Section:
The Large Marsquake of Sol 1222

Evaluation of S1222a Source Parameters Based on Site Effect Simulation and Implication for the Event Origin

Wanbo Xiao[1,2], Taichi Kawamura[1], Zongbo Xu[1], Sebastián Carrasco[3], Keisuke Onodera[4], Grégory Sainton[1], Philippe Lognonné[1], Yanbin Wang[2], Brigitte Knapmeyer-Endrun[3], and William Bruce Banerdt[5]

[1]Université Paris Cité, Institut de physique du globe de Paris, CNRS, Paris, France, [2]Department of Geophysics, School of Earth and Space Sciences, Peking University, Beijng, China, [3]Bensberg Observatory, University of Cologne, Bergisch Gladbach, Germany, [4]Earthquake Research Institute, The University of Tokyo, Tokyo, Japan, [5]Jet Propulsion Laboratory, California Institute of Technology, Pasadena, CA, USA

Abstract Estimating the rupture process of a quake constrains the tectonic setting of its source region. In terrestrial seismology, the rupture process can be described with a classical ω^2 model. In this study, we focus on one key source parameter of S1222a, the corner frequency, to investigate its origin. However, estimating the corner frequency of S1222a is complicated by S1222a's non-classical spectra which deviate from the ω^2 model. To explain S1222a's spectra, we take into account the site effect at the InSight landing site. Through numerical simulation, we demonstrate that the spectral fitting is greatly improved after considering the site effect. We further estimated the source spectrum and stress drop of S1222a. The obtained stress drop resembles the values for regional tectonic earthquakes and shallow moonquakes but differs from the Cerberus Fossae marsquakes, which favors a different tectonic origin from the Cerberus Fossae marsquakes for S1222a.

Plain Language Summary The source of a quake is a key piece of information to uncover the dynamic process at the source region. In terrestrial seismology, the source of a quake can be described with a classical model in which the spectra decay with frequency at a certain speed. In this study, we focus on one key source parameter of S1222a, the corner frequency, to explore the generating process of S1222a. However, S1222a exhibits non-classical spectra which cannot be explained by the classical model, making it difficult to estimate S1222a's source spectrum. To explain S1222a's spectra, we hypothesized that the seismic records are contaminated by wave reverberations in the subsurface layers, namely site effect. We validated our hypothesis with a numerical method. After considering site effect, S1222a's source spectrum and stress drop can be better estimated. The obtained stress drop value is close to those for regional tectonic earthquakes and shallow moonquakes but differs from the values observed for some marsquakes located at Cerberus Fossae, a seismically active region on Mars. Thus, we conclude that S1222a has a different tectonic origin from the Cerberus Fossae marsquakes.

Key Points:

- We constructed a numerical model to simulate the site effect at the InSight landing site to better explain the spectra of S1222a
- We estimated the corner frequency of S1222a to be 0.76 (0.58–1.07) Hz, which corresponds to a stress drop of 3.62 (0.80–20.26) MPa
- The corner frequency and stress drop estimation favor that S1222a has a different tectonic origin from the Cerberus Fossae marsquakes

Supporting Information:

Supporting Information may be found in the online version of this article.

Correspondence to:

W. Xiao,
wxiao@ipgp.fr;
wbxiao@pku.edu.cn

Citation:

Xiao, W., Kawamura, T., Xu, Z., Carrasco, S., Onodera, K., Sainton, G., et al. (2023). Evaluation of S1222a source parameters based on site effect simulation and implication for the event origin. *Geophysical Research Letters*, *50*, e2023GL103429. https://doi.org/10.1029/2023GL103429

Received 24 FEB 2023
Accepted 28 JUN 2023

1. Introduction

Studying the source characteristics of marsquakes can not only help to reveal the current geological features and thermal state (temperature and pressure) of the marsquake source regions, but also provide information on the evolution history of the corresponding regions. NASA's InSight (Interior Exploration using Seismic Investigations, Geodesy and Heat Transport) mission (Banerdt et al., 2020; Banfield et al., 2020; Lognonné et al., 2020) has revealed that Mars is seismically active today, with many of the marsquakes located in Cerberus Fossae (Giardini et al., 2020; Stähler et al., 2022). Centroid moment tensor inversion was applied to some of these marsquakes (Brinkman et al., 2021; Jacob et al., 2022; Sita & van der Lee, 2022). However, the tectonic setting, such as fault movement, magmatic activity, or mass wasting, in most regions of Mars remains to be discovered, which relies on the analyses of marsquakes in the regions of interest.

The source characteristics of a marsquake are described by its source spectrum, such as the classical ω^2 model in terrestrial seismology (Aki & Richards, 2002), in which the seismic spectra decay with frequency by the power of 2. Spectral analysis is a classical technique to constrain the source spectrum of a quake, and to estimate the seismic spectra as a key parameter. Corner frequency estimation is commonly applied to investigate the source features of a quake (e.g., Boatwright, 1984; Brune, 1970; Madariaga, 1976). On Earth, corner frequency estimation has been conducted for different regions to estimate the stress drops at source regions (e.g., Allmann &

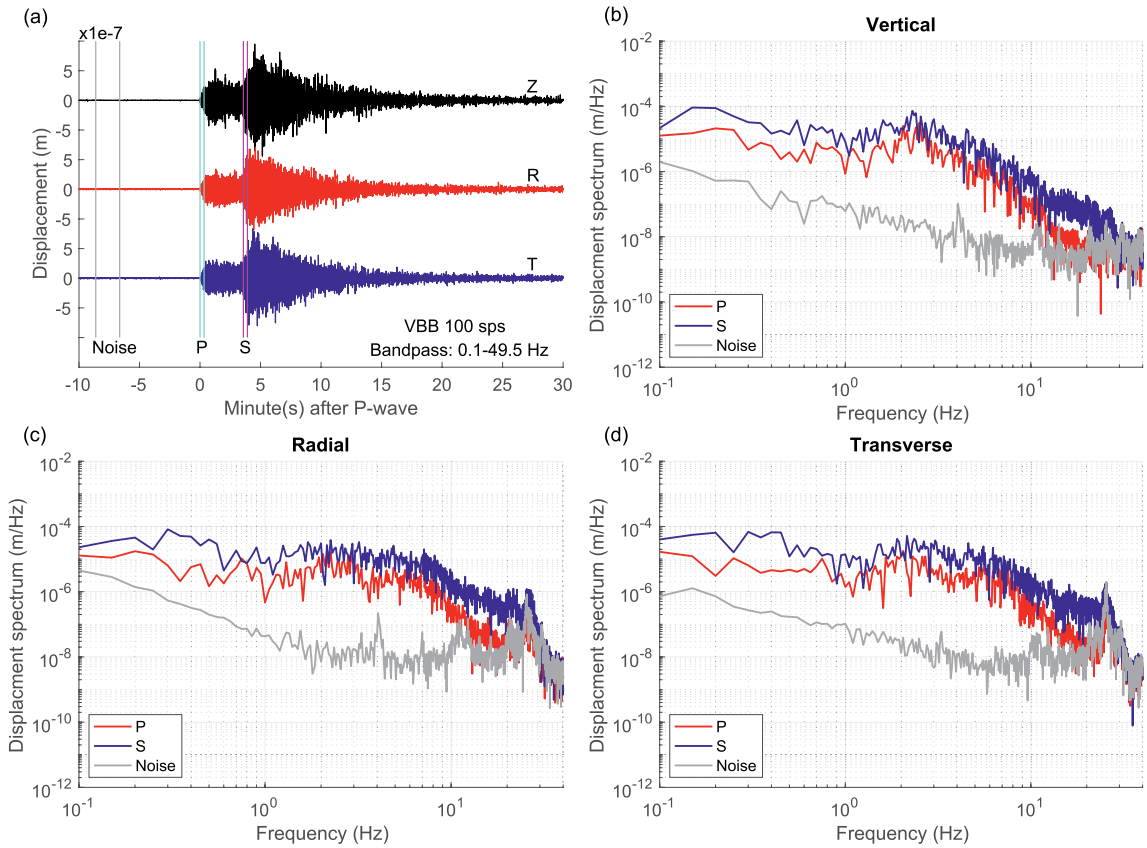

Figure 1. (a) Three-component displacement waveforms and Fourier amplitude spectra for the (b) vertical, (c) radial, and (d) transverse components of S1222a. We used the whole noise spectral window and the first 20 s of the P-wave and S-wave spectral windows of the MQS (InSight Marsquake Service, 2023) for the calculation of the spectra, as marked by the colored vertical lines. The P-wave and S-wave spectra are computed using the marked 20-s windows and the noise spectrum is computed using a 20-s sliding window with 80% overlap.

Shearer, 2009; Baltay et al., 2011; Humphrey & Anderson, 1994; Mori et al., 2003). On the Moon, the corner frequencies of both shallow and deep moonquakes were estimated along with the stress drops and energy release to investigate the origin of these moonquakes (Goins et al., 1981; Kawamura et al., 2017; Oberst, 1987). On Mars, the corner frequencies of several low-frequency (LF) and high-frequency (HF) marsquakes (details of the InSight event definitions are given in Clinton et al., 2021) were analyzed to constrain the tectonic setting in their source region, Cerberus Fossae (Stähler et al., 2022). The marsquake service (MQS, InSight Marsquake Service, 2023) reported that S1222a has a very high signal-to-noise ratio (SNR) in a wide frequency range (Kawamura et al., 2022), which is a natural advantage over other marsquakes when trying to estimate the corner frequency. Accordingly, the source characteristics of such an energetic seismic event will provide an important constraint on the dynamics of Mars' seismicity.

S1222a is the largest event (M_w 4.7) detected by the SEIS (Seismic Experiment for Interior Structure) seismometers (Lognonné et al., 2019) of the InSight mission. S1222a is located to the south of Cerberus Fossae and near the Martian crustal dichotomy, with an epicentral distance of about 37° (Kawamura et al., 2022). A topographic map (Smith et al., 2003) is shown in Figure S1 in Supporting Information S1 and more information of S1222a is contained in Text S1 in Supporting Information S1. One notable feature of S1222a is that the displacement spectral amplitudes increase at frequencies above 1 Hz (Figure 1 of this study or Figure 1 of Kawamura et al. (2022)). This is observed for S1222a more clearly than any other previous events because of S1222a's high SNR at high frequencies. This non-classical spectral feature cannot be explained by the classical ω^2 model of terrestrial seismology (Aki & Richards, 2002). Accordingly, the influence of additional factors, such as the local site effect and/or lander modes (Dahmen et al., 2021; Hurst et al., 2021), on the seismic spectrum is non-negligible.

Site effect usually refers to the frequency-dependent amplification of ground motions induced by shallow low-velocity layers (e.g., Towhata, 2008). The InSight landing site is at the degraded crater *Homestead Hollow*,

which was proposed to be covered by unconsolidated regolith, coarse ejecta, and fractured basaltic lava flows (Golombek et al., 2020; Morgan et al., 2018). In such a geological condition, ground motions are likely influenced by the site effect from these shallow layers. Subsurface models of the landing site have been proposed in previous studies using different approaches (Carrasco et al., 2023a; Hobiger et al., 2021; Onodera, 2022; Xu et al., 2022). These models all include the surface regolith layer but differ with regard to deeper layers. Onodera (2022) and Xu et al. (2022) both showed models where seismic-wave velocity increases with depth. Hobiger et al. (2021) proposed a subsurface structure with a low-velocity layer sandwiched between layers of higher velocities, while Carrasco et al. (2023a) presented models characterized by a high-velocity layer over a low-velocity layer with shallower depths than the models of Hobiger et al. (2021) (see Text S2 in Supporting Information S1 for more details). Recent works based on ellipticity of Rayleigh waves and receiver functions have proposed an interface at about 2 km depth (Carrasco et al., 2023b; Shi et al., 2022). On the other hand, no studies have utilized these models to constrain the site effect and the source spectra of InSight marsquakes. These subsurface models will enable us to quantitatively evaluate the influence of the site effect on the observed spectra, and thus improve the analysis and interpretation of InSight marsquake spectra.

In this study, we present a quantitative estimation of the site effect at the InSight landing site to explain the non-classical spectral features of S1222a and to better constrain S1222a's source spectrum. In Section 2, we present the spectra of S1222a and introduce our numerical method and the models used to simulate the site effect at the InSight landing site. In Section 3, we present the modelled site effect in comparison with the observations for S1222a and the corner frequency estimation after considering the site effect. In Section 4, we discuss the factors influencing our results and the implications of our results for understanding the origin of S1222a.

2. Data and Method

2.1. Spectra of S1222a

In this subsection, we analyze the spectral characteristics of S1222a. Since the short period (SP) sensors were turned off due to a lack of power for the spacecraft, we used the 100-sps VBB data for the spectral analysis (InSight Mars SEIS Data Service, 2019b). We first removed the instrument response of the raw data to get the displacement records, and then rotated the records from U, V, and W components to Z, R, and T components based on the back azimuth of 101° (Kawamura et al., 2022). Then we calculated the Fourier amplitude spectra of the three-component displacements for different time windows based on the noise, P-wave and S-wave spectral window timing provided by the MQS (InSight Marsquake Service, 2023).

The seismic event spectra are well above the noise spectra up to about 20 Hz for P wave and up to 30 Hz for S wave on all three components (Figure 1). Wind-induced lander shaking is a strong contamination of the InSight records at high frequencies (Dahmen et al., 2021; Hurst et al., 2021; Xiao & Wang, 2022), but S1222a has a high enough SNR at high frequencies to ignore the lander shaking. Nevertheless, there is an obvious peak centered at around 25 Hz in the S-wave spectra, which is also visible in the noise and P-wave spectra. The similar amplitudes of the 25 Hz signal in noise and seismic spectra indicate a non-seismic origin. Therefore, we focus the spectral analysis on frequencies between 0.1 and 20 Hz.

The spectra of the first 20-s time windows differ from those of the following time windows and the mean spectra of the whole MQS spectral window (Figure S3 in Supporting Information S1), which indicates that P- and S-wave might be contaminated by scattering effects. Therefore, we used the spectra of the first 20 s that best represent the direct waves for the spectral analyses.

As mentioned before, the major difficulty of estimating the corner frequency of S1222a is the spectral increase starting at around 1.0 Hz, which does not follow the classical ω^2 model nor attenuation models. Such enhancement of energy can also be observed for other smaller HF marsquakes (e.g., Figure S4 in Supporting Information S1 of this study or S0260a in Figure 4 of Stähler et al. (2022)) and was not investigated in depth so far, but it is likely that these marsquakes are also influenced by site effect. Another interesting feature of the S1222a spectra is that the S-wave spectrum decays slower than the P-wave spectrum at high frequencies, which cannot be explained by the intrinsic attenuation scaling relationship $Q_P = \frac{9}{4}Q_S$ (for a Poisson medium where $V_P/V_S = \sqrt{3}$ in Stähler et al. (2022)). This could suggest that the attenuation is more controlled by scattering, for which a higher attenuation of the P wave can be observed (Hong, 2004). Whether these non-classical spectral features of

S1222a can be explained by considering the site effect is worth investigation. To give a quantitative estimation of the site effect, we adopted a similar approach as used in the site effect simulation at the Apollo landing site (Amrouche et al., 2022) to construct numerical models of the InSight landing site. In the next subsection, we present the theoretical basis of our analyses and the design of our numerical experiments to simulate the site effect.

2.2. Synthetic Method

The observed spectra $A(f)$ can be expressed as the combination of the source spectrum $A^{Source}(f)$, attenuation $\exp\left(-\frac{\pi f t}{Q}\right)$ and local site effect $A^{SiteEffect}(f)$, where Q is the attenuation quality factor and t is the travel time. We assume that the source spectrum of S1222a, $A^{Source}(f)$, has the general form of terrestrial seismology (Aki & Richards, 2002) in Equation 1.

$$A^{Source}(f) = \frac{\Omega_0}{\left[1 + (f/f_c)^{\gamma n}\right]^{1/\gamma}} \tag{1}$$

where f_c is the corner frequency, Ω_0 is the DC spectrum (spectral amplitude at zero frequency).

The observed spectra $A(f)$ can be written as

$$A(f) = \frac{\Omega_0}{\left[1 + (f/f_c)^{\gamma n}\right]^{1/\gamma}} \times \exp\left(-\frac{\pi f t}{Q}\right) \times A^{SiteEffect}(f) \tag{2}$$

The Brune (1970) model indicates $\gamma = 1$ and $n = 2$ while $n = 2.5$ is used in Stähler et al. (2022) for elongated faults.

As shown in Equation 2, the source spectrum and attenuation are constrained by the decay of the spectral energy at high frequencies, so it is critical to quantitatively evaluate the influence of the site effect at high frequencies, and numerical modeling is one effective way to achieve this.

To compute the synthetic seismograms for a number of layers over a half-space, which is the current knowledge of the subsurface structure at the InSight landing site, we adopted the reflectivity method (Fuchs & Müller, 1971; Müller, 1985). This method analytically solves the body-wave reflection and transmission equations in a laterally homogeneous velocity model. The advantage of applying the reflectivity method is that it can easily calculate the synthetic spectra up to a high frequency (e.g., 50 Hz) and that its efficient computation greatly reduces the computational demands in cases of large layered models, as its CPU load is not related to the layer thicknesses.

The sketch map of our simulation model is given in Figure S5 of Supporting Information S1. We used a point source that radiates transient P- and SV-energy, with the source spectrum being flat to exclude its influence on the simulation. The source is located vertically beneath the surface receiver (Figure S5 in Supporting Information S1), with a depth of 90 km in order to have a sufficiently large arrival time difference for the direct P and S waves. We tested that the source depth has no significant influence on the main features of the synthetic spectra (Figure S6 in Supporting Information S1). In our simulation, we mainly focus on the P vertical and S radial components since the synthetic seismic wavefield is predominantly propagating along the vertical direction. We have validated our site effect computation using the analytical equation of two-layer models (Figure S7 in Supporting Information S1). The sample rate is set to 100 Hz (Nyquist frequency 50 Hz) so as to also investigate the site effect at high frequencies and to be fully comparable to the VBB data. We selected a 20-s time window starting from the P or S arrival to calculate the corresponding synthetic spectra.

2.3. Subsurface Models

We set up our simulation model as a number of shallow layers over a half-space following previous studies. The shallow layers are set to be the subsurface models proposed by previous studies obtained from different approaches (Carrasco et al., 2023a; Hobiger et al., 2021; Onodera, 2022; Xu et al., 2022). For the half-space, the S-wave velocity is set to 1.5 km/s based on the reference value from receiver function analyses (1.2–2.1 km/s, Carrasco et al., 2023b; Knapmeyer-Endrun et al., 2021; Lognonné et al., 2020) and the P-wave velocity is set to 2.6 km/s assuming a V_p/V_s ratio of 1.73 for a Poisson solid (Giardini et al., 2020; Stähler et al., 2022). We

select one representative model, the best M1 model of Carrasco et al. (2023a) (hereafter SCM1), to present the improvement of the spectral fitting of S1222a by applying our method. The SCM1 model (Carrasco et al., 2023a) was obtained from the horizontal to vertical spectral ratio (HVSR, Nakamura, 1989; Nogoshi & Igarashi, 1971) inversion of marsquake S-coda waves including the 2.4 Hz mode and assuming a reasonable value for the maximum S-wave velocity in the topmost 100 m (below 1500 m/s). Details of each subsurface model and a comparison between these models are provided in Text S2 and Figure S2 in Supporting Information S1. The attenuation quality factors in all layers are set to a very high value (10^5) to exclude the attenuation effect. Since the corner frequency and attenuation are not included in our simulation, the synthetic spectra represent the site effect from the subsurface layers, which can be easily compared with the observations for S1222a to investigate the origin of the spectral increase at 1 Hz.

3. Results

3.1. Spectral Fitting

The predominant features of the synthetic spectra do not change significantly between different models, so we only present the results for the SCM1 model in the main text and provide details on the results for other models in the Supporting Information S1 (Figure S8).

The comparison between the synthetic spectra of the model SCM1 and the observations for S1222a is displayed in Figure 2. The synthetic spectra are normalized by optimizing the fitting with the observed spectra in the frequency range 0.1–0.3 Hz, where the influence of the site effect is modest and the spectra are almost flat. The synthetic P-wave vertical (PV) spectrum (Figure 2, blue curves) exhibits a wide peak between 1 and 6 Hz which matches with the non-classical spectral shape of the observed S1222a PV spectrum. For the S-wave radial (SR) spectrum, the general trend of the synthetics is similar to the observation, although the peak at 1.4 Hz in the synthetics is not obvious in the observations. These comparisons confirm the possibility that the site effect from the subsurface layers can be the origin of the non-classical spectral increase in the observations for S1222a. Such a consistency also inspires us to further investigate whether the whole spectra of S1222a can be explained by Equation 2 after considering the site effect.

3.2. Grid Search for Corner Frequency

With the site effect taken into account, a simple grid search method enables us to simultaneously determine the corner frequency and quality factor using Equation 2. We used the following misfit function for the grid search (Equation 3) and conducted frequency resampling on a logarithmic scale to balance the fitting of low frequencies and high frequencies.

$$\Phi^{P,S} = \sqrt{\sum_f \left[\log_{10}\left(Obs^{P,S}(f)\right) - \log_{10}\left(Syn^{P,S}(f)\right)\right]^2} \tag{3}$$

where $Obs^{P,S}(f)$ and $Syn^{P,S}(f)$ denote the observed and synthetic spectrum at frequency f, respectively, for P or S wave. We search for the corner frequency $fc^{P,S}$ between 0.1 and 10 Hz with a logarithmically linear interval of $10^{0.01}$ and the quality factor $Q^{P,S}$ between 100 and 1,00,000 with a logarithmically linear interval of $10^{0.02}$. We conducted the grid search for PV and SR spectra individually to determine the corner frequencies and attenuation quality factors of P and S waves. After we obtained the values from the individual grid searches, we refer to the scaling relationships $f_c^S / f_c^P = \frac{0.21}{0.32}$ (Madariaga, 1976) and $Q_P = \frac{9}{4} Q_S$ (Stähler et al., 2022) to test whether the values match with the other spectrum.

The spectral fitting is greatly improved by applying the grid search (red and cyan curves in Figures 2a and 2b). Benefiting from the high SNR of S1222a in a wide frequency range, we are able to separate the site effect from other factors, such as the source spectrum and attenuation (Figures 2c and 2d). The site effect causes the spectral increase while both the corner frequency and attenuation induce the spectral decay, jointly resulting in the unique spectral shape of S1222a. The optimal pair lines (cyan curves) in the misfits of the grid searches (Figures 2e and 2f) represent the trade-off between the corner frequency and quality factor. We define the uncertainty of the results as the 95% confidence intervals along the optimal pair lines. For the Brune (1970) model ($n = 2.0$), the P-wave corner frequency (and uncertainty) lies around 0.76 Hz (0.58–1.07 Hz) and the attenuation quality

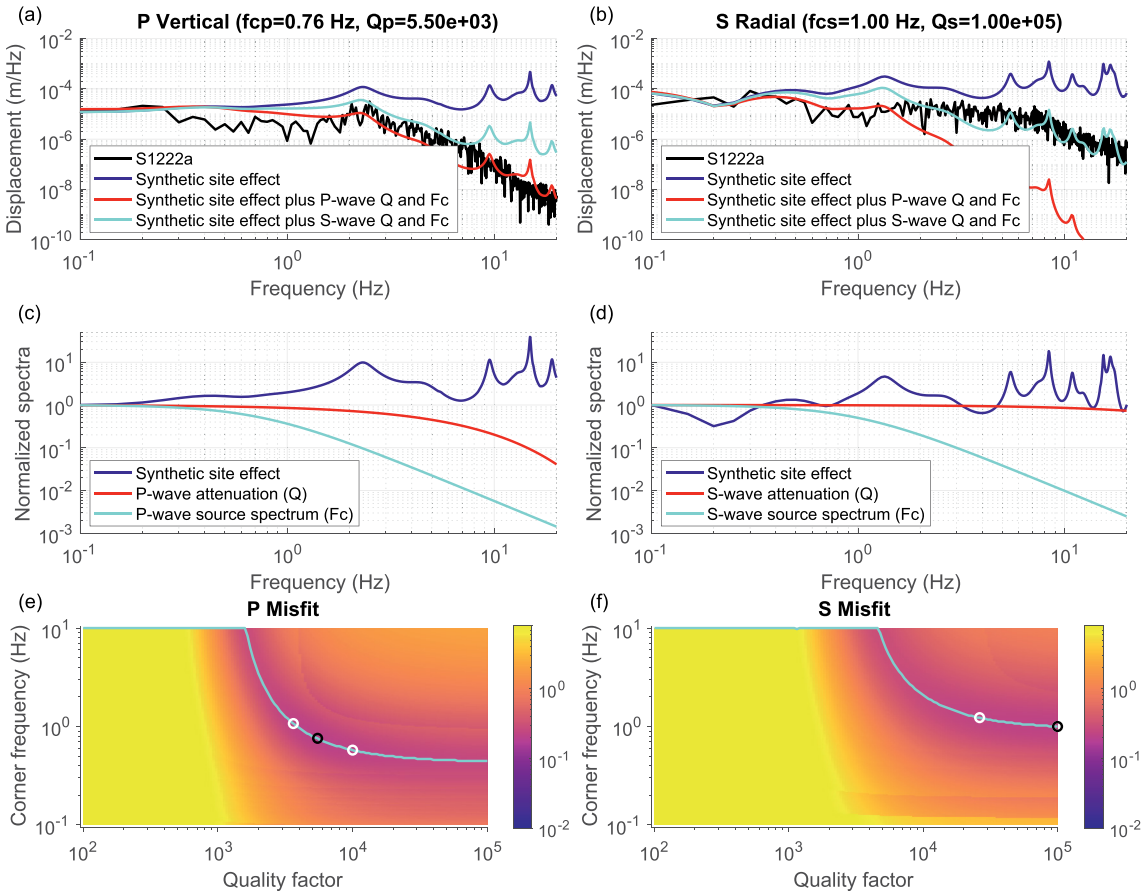

Figure 2. Fitting of the Fourier amplitude spectra of S1222a using the Brune (1970) model ($n = 2.0$). The top two panels show the spectral fittings of (a) P-wave vertical and (b) S-wave radial components. The black curves are the observed spectra of S1222a. The original synthetic spectra are in blue while the synthetic spectra including the corner frequency and attenuation are in red and cyan. The P-wave vertical and S-wave radial spectra are used to obtain the source parameters of P and S waves, respectively. Then we refer to the scaling relationships $f_c^S / f_c^P = \frac{0.21}{0.32}$ (Madariaga, 1976) and $Q_P = \frac{9}{4} Q_S$ (for a Poisson medium where $V_P/V_S = \sqrt{3}$, Stähler et al., 2022) to test whether the values from the individual grid searches also match the other spectrum. The middle two panels show the normalized spectra of the synthetic site effect, attenuation and source spectrum in Equation 2 for the (c) P-wave vertical and (d) S-wave radial components, using the results from the grid searches. The bottom two panels show the misfits of the grid searches for the (e) P-wave vertical spectrum and (f) S-wave radial spectrum. The cyan lines mark the optimal pairs of values for the corner frequency and attenuation quality factor. The black and white circles mark the minimum misfits and the 95% confidence intervals along these lines, respectively.

factor is around 5,500 (3,630–10,000). For S wave, the corner frequency is slightly larger (1.00–1.23 Hz) and the attenuation quality factor is poorly constrained (over 26,300). We will further discuss the implications of these estimates in the next section.

4. Discussion

4.1. Implications From P-Wave Spectral Fitting

Stähler et al. (2022) investigated the corner frequencies of several marsquakes in Cerberus Fossae. They found that the estimated corner frequencies are between 0.45 and 0.95 Hz for the LF events and above 1.5 Hz for the HF events, which is lower than the typical values for earthquakes with similar magnitudes. The following relationship between the corner frequency f_c and stress drop $\Delta\sigma$ (Equation 4) is used in Stähler et al. (2022) to compare the source parameters of earthquakes, moonquakes, and marsquakes.

$$f_c = k\beta \sqrt[3]{\frac{16}{7} \frac{\Delta\sigma}{M_0}} \tag{4}$$

where β is the shear wave velocity, M_0 is the seismic moment, and k is a scaling parameter. If we select the same parameter values as used in Stähler et al. (2022) (3 km/s for β and $k = 0.38$ for P wave, Kaneko & Shearer, 2014)

Table 1
Stress Drop Estimation From S1222a P Wave in Comparison With Other Quakes

Data	$\Delta\sigma$ (MPa)	f_c (Hz)
Grid search of S1222a in this study		
Using the Brune (1970) model ($n = 2.0$)	3.62 (0.80–20.26)	0.76 (0.58–1.07)
Using the elongated fault model ($n = 2.5$)	21.73 (4.13–132.30)	1.38 (1.00–2.00)
Results of other quakes		
Guerrero subduction zone earthquakes (Humphrey & Anderson, 1994)	0.5–85	0.18–11.20
Southern California earthquakes (Mori et al., 2003)	0.5–75	/
Japan earthquakes (Baltay et al., 2011)	0.1–30	0.3–3
Shallow moonquakes (Oberst, 1987)	0.5–210	0.43–6.11
General LF marsquakes (Stähler et al., 2022)	0.1–10	0.23–1.70
Cerberus Fossae marsquakes (Stähler et al., 2022)	0.001–0.1	0.05–0.37

Note. To estimate the stress drop of S1222a, we applied Equation 4 and used the seismic moment range of S1222a $1.4 \times 10^{16}(7.0 \times 10^{15} - 2.8 \times 10^{16})$ N m given in Kawamura et al. (2022), 3 km/s for β and $k = 0.38$ for P wave (Kaneko & Shearer, 2014). Other values are obtained from previous studies for the seismic moment range of S1222a.

and take the seismic moment of S1222a (1.4×10^{16}N m, Kawamura et al., 2022), we obtain a stress drop of 3.62 (1.61–10.13) MPa corresponding to the estimated P-wave corner frequency 0.76 (0.58–1.07) Hz. The uncertainty of the seismic moment of S1222a ($7.0 \times 10^{15} - 2.8 \times 10^{16}$N m) will extent the stress drop range to 0.80–20.26 MPa. We summarized the stress drops of different earthquakes, moonquakes, and marsquakes from previous studies in Table 1. In comparison to the large variety of observations on Earth and the Moon, the corner frequency and stress drop estimates of S1222a are consistent with the values for regional tectonic earthquakes and shallow moonquakes when within the seismic moment range of S1222a. On the other hand, our estimated stress drop for S1222a is higher than the values measured for the Cerberus Fossae marsquakes (Stähler et al., 2022). While Stähler et al. (2022) proposed a magmatic origin for the Cerberus Fossae marsquakes to explain the observed low stress drops, our result for S1222a favors a higher stress drop which is more in line with terrestrial tectonic quakes. This might also be supported by the MQS location of S1222a which is outside the Cerberus Fossae region (Kawamura et al., 2022).

We notice that different n values in Equation 1 may introduce uncertainty to the stress drop estimation (e.g., Abercrombie, 2021; Neely et al., 2020). If we take $n = 2.5$ for elongated faults (Stähler et al., 2022), the estimated P-wave corner frequency is larger (1.38, 1.00–2.00 Hz), corresponding to a larger stress drop of 21.73 (4.13–132.30) MPa (Figure S9 in Supporting Information S1), although the attenuation is barely constrained. The P-wave attenuation quality factor is fixed (2,250) in the analyses of Stähler et al. (2022), which corresponds to a high corner frequency and thus a high stress drop in Figure 2. Besides, another influencing factor is that Stähler et al. (2022) did not consider the site effect, although the LF marsquakes in Cerberus Fossae are less affected by the high-frequency site effect. While further investigations need to be made, our result favors a different origin for S1222a compared to the Cerberus Fossae marsquakes.

The P-wave attenuation quality factor (3,630–10,000) is larger than the previous estimates for the Martian crust (e.g., around 1,500 for S0173a and S0235b in Cerberus Fossae, Lognonné et al., 2020). The effective attenuation along the ray path of S1222a includes both intrinsic and scattering attenuation. The intrinsic attenuation quality factor of the Martian crust is found to be relatively large compared to the scattering attenuation quality factor, and the scattering attenuation is frequency-dependent (Lognonné et al., 2020; Menina et al., 2021; van Driel et al., 2021). In this study, we used a constant quality factor so as to have a better comparison with Stähler et al. (2022), while the frequency-dependent attenuation could be one way to improve the attenuation estimation in future studies.

4.2. Less Effective S-Wave Spectral Fitting

While the P-wave spectrum can be well reproduced with the source spectrum, attenuation and site effect, we observed significant differences between the synthetics and observation for the S-wave spectrum. Furthermore,

the estimated corner frequency and attenuation quality factor for S wave are higher than the P-wave values. The SR spectrum above 2 Hz can be roughly fitted, while the obviously mismatched parts are between 1 and 2 Hz and below 0.5 Hz. Theoretically, the synthetic peaks caused by the wave reverberations in the shallow layers are related to both the seismic wave velocities and thicknesses of the shallow layers. So the synthetic SR spectrum presents a peak at around 1.4 Hz peak which corresponds to the 2.4 Hz peak of the synthetic PV spectrum. The difference between the synthetic and observed SR spectra implies that the simple models that we proposed here have some missing elements and cannot fully explain the observed S-wave spectrum.

We propose here some possibilities for elements that we might be missing in our models. First, from the perspective of the simulation, we simulated the site effect under the condition of vertical incidence, while the incidence angle of S1222a is not exactly vertical in practice. From our tests of the incidence angles (Figure S10 in Supporting Information S1), the shape of the SR spectrum changes slightly for different incidence angles, which is not enough to explain the difference we observed, so we can exclude this possibility. Second, the scattering is not considered in the synthetics. This will likely change the energy partitioning of Z and R components, which also influences the spectral shapes. From the perspective of observations, although we used the first 20 s of the MQS spectral windows to calculate the spectra of the direct waves, the direct S wave might be contaminated by P coda (Figure S3 in Supporting Information S1). We also recall here the interesting observation that the S-wave spectrum decays slower than the P-wave spectrum at high frequencies, which is the opposite of the empirical relationship $Q_P = \frac{9}{4}Q_S$ and cannot be explained by the site effect simulation. An explanation of the unusual features of S1222a's S-wave spectrum requires more detailed analyses in future studies.

5. Conclusion

The source parameters of a quake reflect the characteristics of the quake's origin. We perform here a quantitative evaluation of site effect to better constrain the source spectrum evaluation. This allows us an improved estimation of the corner frequency that is contaminated by site effect. The corner frequency of S1222a provides information about its origin process and has implications for the tectonics at its location near the Martian crustal dichotomy. S1222a, as the largest InSight event, exhibits a very high SNR in a wide frequency range that is beneficial for the corner frequency estimation, but its non-classical spectral increase above 1 Hz cannot be explained by a classical model, such as the ω^2 model, and attenuation. In this study, we propose that the observed spectra might be influenced by the local site effect from the subsurface layers. We then design numerical experiments to simulate the synthetic site effect in a model consisting of homogeneous layers over a half-space. We test different subsurface models from previous studies and find that considering the synthetic site effect greatly improves the spectral fitting of S1222a. This confirms that the S1222a spectra are significantly influenced by the local site effect. Using our numerical model, we are able to correct the spectra with the predicted site effect and then estimate the corner frequency and attenuation using a grid search method. The estimated corner frequency and stress drop from the P-wave spectrum and seismic moment of S1222a are consistent with the scaling relationship for regional tectonic earthquakes and shallow moonquakes, while the stress drop estimate of S1222a is higher than those for the Cerberus Fossae marsquakes. This might indicate a different origin for S1222a compared to the Cerberus Fossae marsquakes. On the other hand, we observe a significant discrepancy between the synthetic and observed S-wave spectrum. This may indicate that our simulation models are not sufficient to explain the observed S-wave spectrum and further in-depth investigations are required. Our study for the first time gives a quantitative estimation of the site effect of S1222a, which provides a reference for future studies concerning the source parameters of S1222a and other InSight events.

Data Availability Statement

The InSight seismic data are available from IPGP's MSDC (InSight Mars SEIS Data Service, 2019b), in parallel with the IRIS DMC (Data Management Center, https://www.iris.edu/hq/sis/insight) and the NASA's PDS (Planetary Data System, https://pds-geosciences.wustl.edu/missions/insight/seis.htm; InSight Mars SEIS Data Service, 2019a). The Mars seismic catalog can be found in InSight Marsquake Service (2023).

Acknowledgments
The authors acknowledge NASA, CNES, their partner agencies and Institutions (UKSA, SSO, DLR, JPL, IPGP-CNRS, ETHZ, IC, and MPS-MPG), and the flight operations team at JPL, SISMOC, MSDS, IRIS-DMC, and PDS for providing SEED SEIS data (InSight Mars SEIS Data Service, 2019a, 2019b). Under this reference all access to the SEIS data archives can be found. The authors thank editor Kevin Lewis, reviewer Rachel E. Abercrombie and another anonymous reviewer for providing very helpful comments that improved the manuscript. WX acknowledges the Natural Science Foundation of China (NSFC) No. 41930103 and CSC scholarship No. 202106010143. French co-authors acknowledge the support of the French Space Agency CNES and Agence Nationale de la Recherche, ANR (ANR-19-CE31-0008-08). TK, MP, PL, GS acknowledge the support of IdEx Université Paris Cité ANR-18-IDEX-0001. This research was carried out in part at the Jet Propulsion Laboratory, California Institute of Technology, under a contract with the National Aeronautics and Space Administration (80NM0018D0004). This paper is InSight Contribution Number 289.

References

Abercrombie, R. E. (2021). Resolution and uncertainties in estimates of earthquake stress drop and energy release. *Philosophical Transactions Royal Society A*, *379*(2196), 20200131. https://doi.org/10.1098/rsta.2020.0131

Aki, K., & Richards, P. (2002). The seismic source: Kinematics. In J. Ellis (Ed.), *Quantitative seismology* (2nd ed., pp. 491–536). University Science Books.

Allmann, B., & Shearer, P. (2009). Global variations of stress drop for moderate to large earthquakes. *Journal of Geophysical Research*, *114*(B1), B01310. https://doi.org/10.1029/2008JB005821

Amrouche, M., Weber, R., Schmerr, N., & Iqbal, W. (2022). Effects of lunar near-surface geology on moonquakes ground motion amplification. *Journal of Geophysical Research: Planets*, *127*(9). https://doi.org/10.1029/2022JE007396

Baltay, A., Ide, S., Prieto, G., & Beroza, G. (2011). Variability in earthquake stress drop and apparent stress. *Geophysical Research Letters*, *38*(6), L06303. https://doi.org/10.1029/2011GL046698

Banerdt, W., Smrekar, S., Banfield, D., Giardini, D., Golombek, M., Johnson, C., et al. (2020). Initial results from the InSight mission on Mars. *Nature Geoscience*, *13*(3), 183–189. https://doi.org/10.1038/s41561-020-0544-y

Banfield, D., Spiga, A., Newman, C., Forget, F., Lemmon, M., Lorenz, R., et al. (2020). The atmosphere of Mars as observed by InSight. *Nature Geoscience*, *13*(3), 190–198. https://doi.org/10.1038/s41561-020-0534-0

Boatwright, J. (1984). Seismic estimates of stress release. *Journal of Geophysical Research*, *89*(B8), 6961–6968. https://doi.org/10.1029/JB089iB08p06961

Brinkman, N., Stähler, S., Giardini, D., Schmelzbach, C., Khan, A., Jacob, A., et al. (2021). First focal mechanisms of marsquakes. *Journal of Geophysical Research: Planets*, *126*(4). https://doi.org/10.1029/2020JE006546

Brune, J. (1970). Tectonic stress and the spectra of seismic shear waves from earthquakes. *Journal of Geophysical Research*, *75*(26), 4997–5009. https://doi.org/10.1029/jb075i026p04997

Carrasco, S., Knapmeyer-Endrun, B., Margerin, L., Schmelzbach, C., Onodera, K., Pan, L., et al. (2023). Empirical H/V spectral ratios at the InSight landing site and implications for the martian subsurface structure. *Geophysical Journal International*, *232*(2), 1293–1310. https://doi.org/10.1093/gji/ggac391

Carrasco, S., Knapmeyer-Endrun, B., Margerin, L., Xu, Z., Joshi, R., Schimmel, M., et al. (2023). Constraints for the martian crust structure from Rayleigh waves ellipticity of large seismic events. *Geophysical Research Letters*. https://doi.org/10.22541/essoar.167690105.50345414/v1

Clinton, J., Ceylan, S., van Driel, M., Driel, M., Giardini, D., Stähler, S., et al. (2021). The marsquake catalogue from InSight, sols 0–478. *Physics of the Earth and Planetary Interiors*, *310*, 106595. https://doi.org/10.1016/j.pepi.2020.106595

Dahmen, N., Zenhäusern, G., Clinton, J., Giardini, D., Stähler, S., Ceylan, S., et al. (2021). Resonances and lander modes observed by InSight on Mars (1–9 Hz). *Bulletin of the Seismological Society of America*, *111*(6), 2924–2950. https://doi.org/10.1785/0120210056

Fuchs, K., & Müller, G. (1971). Computation of synthetic seismograms with the reflectivity method and comparison with observations. *Geophysical Journal International*, *23*(4), 417–433. https://doi.org/10.1111/j.1365-246X.1971.tb01834.x

Giardini, D., Lognonné, P., Banerdt, W., Pike, W., Christensen, U., Ceylan, S., et al. (2020). The seismicity of Mars. *Nature Geoscience*, *13*(3), 205–212. https://doi.org/10.1038/s41561-020-0539-8

Goins, N., Danity, A., & Toksöz, M. (1981). Seismic energy release of the Moon. *Journal of Geophysical Research*, *86*(B1), 378–388. https://doi.org/10.1029/JB086iB01p00378

Golombek, M., Warner, N., Grant, J., Hauber, E., Ansan, V., Weitz, C., et al. (2020). Geology of the InSight landing site on Mars. *Nature Communication*, *11*(1014), 1014. https://doi.org/10.1038/s41467-020-14679-1

Hobiger, M., Hallo, M., Schmelzbach, C., Stähler, S., Fäh, D., Giardini, D., et al. (2021). The shallow structure of Mars at the InSight landing site from inversion of ambient vibrations. *Nature Communication*, *12*(1), 6756. https://doi.org/10.1038/s41467-021-26957-7

Hong, T. (2004). Scattering attenuation ratios of P and S waves in elastic media. *Geophysical Journal International*, *158*(1), 211–224. https://doi.org/10.1111/j.1365-246X.2004.02298.x

Humphrey, J. R., & Anderson, J. G. (1994). Seismic source parameters from the Guerrero subduction zone. *Bulletin of the Seismological Society of America*, *84*(6), 1754–1769. https://doi.org/10.1785/BSSA0840061754

Hurst, K., Fayon, L., Knapmeyer-Endrun, B., Schmelzbach, C., van Driel, M., Ervin, J., et al. (2021). Resonances of the InSight seismometer on Mars. *Bulletin of the Seismological Society of America*, *111*(6), 2951–2963. https://doi.org/10.1785/0120210137

InSight Mars SEIS Data Service. (2019b). SEIS raw data, InSight mission. *IPGP, JPL, CNES, ETHZ, ICL, MPS, ISAE-Supaero, LPG, MFSC*. https://doi.org/10.18715/SEIS.INSIGHT.XB_2016

InSight Marsquake Service. (2023). Mars seismic catalogue, InSight mission; V13 2023-01-01. ETHZ, IPGP, JPL, ICL, Univ. Bristol Retrieved from https://www.insight.ethz.ch/seismicity/catalog/v13

InSight Mars SEIS Data Service. (2019a). Data service, InSight SEIS data Bundle. *PDS Geosciences (GEO) Node*. https://doi.org/10.17189/1517570

Jacob, A., Plasman, M., Perrin, C., Fuji, N., Lognonné, P., Xu, Z., et al. (2022). Seismic sources of InSight marsquakes and seismotectonic context of Elysium Planitia, Mars. *Tectonophysics*, *837*, 229434. https://doi.org/10.1016/j.tecto.2022.229434

Kaneko, Y., & Shearer, P. M. (2014). Seismic source spectra and estimated stress drop derived from cohesive-zone models of circular subshear rupture. *Geophysical Journal International*, *197*(2), 1002–1015. https://doi.org/10.1093/gji/ggu030

Kawamura, T., Clinton, J., Zenhäusern, G., Ceylan, S., Horleston, A., Dahmen, N., et al. (2022). S1222a – The largest marsquake detected by InSight. *Geophysical Research Letters*, *50*(5). https://doi.org/10.1029/2022GL101543

Kawamura, T., Lognonné, P., Nishikawa, Y., & Tanaka, S. (2017). Evaluation of deep moonquake source parameters: Implication for fault characteristics and thermal state. *Journal of Geophysical Research: Planets*, *122*(7), 1487–1504. https://doi.org/10.1002/2016JE005147

Knapmeyer-Endrun, B., Panning, M., Bissig, F., Joshi, R., Khan, A., Kim, D., et al. (2021). Thickness and structure of the martian crust from InSight seismic data. *Science*, *373*(6553), 438–443. https://doi.org/10.1126/science.abf8966

Lognonné, P., Banerdt, W., Giardini, D., Pike, W., Christensen, U., Laudet, P., et al. (2019). Seis: Insight's seismic experiment for internal structure of Mars. *Space Science Reviews*, *215*(1), 12. https://doi.org/10.1007/s11214-018-0574-6

Lognonné, P., Banerdt, W., Pike, W., Giardini, D., Zweifel, P., Garcia, R. F., et al. (2020). Constraints on the shallow elastic and anelastic structure of Mars from InSight seismic data. *Nature Geoscience*, *13*(3), 213–220. https://doi.org/10.1038/s41561-020-0536-y

Madariaga, R. (1976). Dynamics of an expanding circular fault. *Bulletin of the Seismological Society of America*, *66*(3), 639–666. https://doi.org/10.1785/BSSA0660030639

Menina, S., Margerin, L., Kawamura, T., Lognonné, P., Marti, J., Drilleau, M., et al. (2021). Energy envelope and attenuation characteristics of high-frequency (HF) and very-high-frequency (VF) Martian events. *Bulletin of the Seismological Society of America*, *111*(6), 3016–3034. https://doi.org/10.1785/0120210127

Morgan, P., Grott, M., Knapmeyer-Endrun, B., Golombek, M., Delage, P., Lognonné, P., et al. (2018). A pre-landing assessment of regolith properties at the InSight landing site. *Space Science Reviews*, *214*(6), 104. https://doi.org/10.1007/s11214-018-0537-y

Mori, J., Abercrombie, R. E., & Kanamori, H. (2003). Stress drops and radiated energies of aftershocks of the 1994 Northridge, California, earthquake. *Journal of Geophysical Research*, *108*(B11), 2545. https://doi.org/10.1029/2001JB000474

Müller, G. (1985). The reflectivity method: A tutorial. *Journal of Geophysics*, *58*, 153–174.

Nakamura, Y. (1989). A method for dynamic characteristics estimation of subsurface using microtremor on the ground surface. *Railway Technical Research Institute, Quarterly Reports*, *30*(1).

Neely, J. S., Stein, S., & Spencer, B. D. (2020). Large uncertainties in Earthquake stress-drop estimates and their tectonic consequences. *Seismology Research Letters*, *91*(4), 2320–2329. https://doi.org/10.1785/0220200004

Nogoshi, M., & Igarashi, T. (1971). On the amplitude characteristics of microtremor (part 2). *Zisin*, *24*(1), 26–40. https://doi.org/10.4294/zisin1948.24.1_26

Oberst, J. (1987). Unusually high stress drops associated with shallow Moonquakes. *Journal of Geophysical Research*, *92*(B2), 1397–1405. https://doi.org/10.1029/JB092iB02p01397

Onodera, K. (2022). Subsurface structure of the Moon and Mars from 3D seismic wave propagation simulation and analysis of Apollo and InSight seismic data (doctoral dissertation). The Graduate University for Advanced Studies, SOKENDAI and Université Paris Cité. Retrieved from http://id.nii.ac.jp/1013/00006193

Shi, J., Plasman, M., Knapmeyer-Endrun, B., Xu, Z., Kawamura, T., Lognonné, P., et al. (2022). High-frequency receiver functions with event S1222a reveal a discontinuity in the Martian shallow crust. *Geophysical Research Letters*, *50*(5). https://doi.org/10.1029/2022GL101627

Sita, M., & vander Lee, S. (2022). Potential volcano-tectonic origins and faulting mechanisms of three low-frequency marsquakes detected by a single InSight seismometer. *Journal of Geophysical Research: Planets*, *127*, e2022JE007309. https://doi.org/10.1029/2022JE007309

Smith, D., Neumann, G., Arvidson, R. E., Guinness, E. A., & Slavney, S. (2003). Mars Global Surveyor Laser Altimeter mission experiment gridded data record. NASA Planetary Data System, MGS-M-MOLA-5-MEGDR-L3-V1.0.

Stähler, S., Mittelholz, A., Perrin, C., Kawamura, T., Kim, D., Knapmeyer, M., et al. (2022). Tectonics of Cerberus Fossae unveiled by marsquakes. *Nature Astronomy*, *6*(12), 1376–1386. https://doi.org/10.1038/s41550-022-01803-y

Towhata, I. (2008). Dynamic response analysis. In W. Wu & R. Borja (Eds.), *Geotechnical earthquake engineering* (pp. 88–120). Springer-Verlag. https://doi.org/10.1007/978-3-540-35783-4

van Driel, M., Ceylan, S., Clinton, J., Giardini, D., Horleston, A., Margerin, L., et al. (2021). High-frequency seismic events on Mars observed by InSight. *Journal of Geophysical Research: Planets*, *126*, e2020JE006670. https://doi.org/10.1029/2020JE006670

Xiao, W., & Wang, Y. (2022). Characteristics of horizontal to vertical spectral ratio of InSight seismic data from Mars. *Journal of Geophysical Research: Planets*, *127*(6), e2020JE006813. https://doi.org/10.1029/2020JE006813

Xu, Z., Froment, M., Garcia, R., Beucler, E., Onodera, K., Kawamura, T., et al. (2022). Modeling seismic recordings of high-frequency guided infrasound on Mars. *Journal of Geophysical Research: Planets*, *127*(11), e2022JE007483. https://doi.org/10.1029/2022JE007483